Regular article

Modeling the electrical activity of the heart: A Bidomain Model of the ventricles embedded in a torso

Glenn Terje Lines[1,2]**, Per Grøttum**[2]**, Aslak Tveito**[1,2]

[1] Simula Research Laboratory, P.O. Box 134 Lysaker, N-1325, Norway
 (e-mail: glennli@simula.no)
[2] Department of Informatics, University of Oslo, P.O. Box 1080 Blindern, N-0316, Norway

Abstract. In this paper a model for the electrical activity of the heart will be presented and an approach to solve the resulting numerical problem will be suggested. The Bidomain Model is used to compute the spatial distribution of the electrical potential. The partial differential equations are discretized with the finite element method and the multigrid method is used to solve the corresponding linear equations. Adaptivity is applied to resolve the steep gradients in the solution.

1 Introduction

The contraction of the heart is preceded and caused by a cellular electro-chemical reaction. This reaction causes an electrical field to be created. The measurement of this field on the body surface is called the electrocardiogram (ECG). The ECG is an important tool for the clinician in that it changes characteristically in a number of pathological conditions. Infarction and rhythm disturbances are among the illnesses that can be detected by such measurements.

A motivation for simulating the electrical activity in the heart is to gain a better understanding of the relationship between the ECG signal and different anomalies in the heart. For example how does the size and the location of an infarct affect the electrical field generated by the heart?

Mathematically the electrical activity of the heart is described by the Bidomain Model. It was introduced by Geselowitz in the late 70s [8]. On realistic geometries it is not possible to solve these equations analytically. Even numerically these models are hard to solve and one has been forced to sacrifice accuracy in order to obtain any results at all. Using simplified models or solving the equations with coarse discretizations are two options, a third possibility is to simulate only a small portion of the myocardium (the heart muscle). Often a combination of all the three simplifications has been employed.

Important analysis of the model has been performed by Colli Franzone et al. [3–5] including the derivation of the eikonal equation. This formulation makes some simplifying assumptions which greatly reduces the numerical workload.

The eikonal formulation has also been derived independently by Keener [16]. The Bidomain Model includes a term describing the flow of ions across the cell membrane. The simplest ion model describes the current as a cubic function of the potential. This model is commonly used in connection with the Eikonal Model since it makes it possible to obtain a parameter of the model (dimensionless propagation speed) analytically. This is not possible with more complex ionic models, where the parameter must be estimated numerically. Simulations with better ionic models have been performed by Rogers and McCulloch [23] who used the FitzHugh–Nagumo model [7]. More recently Huiskamp [13] has performed simulations using the Beeler–Reuter equations [1]. That study also made use of accurate 3D geometry made available by Hunter et al. [21].

Determining the body surface potential from the heart surface potential is termed the forward problem. It is necessary to also solve this problem in order to compute the surface ECGs. The mathematical model for this problem is simpler than the Bidomain Model for the heart. However, in order to perform realistic simulations the varying conductivities in the torso should be incorporated. The variation in the conductivities are due to inhomogeneities and anisotropic muscle tissue.

In the present work we have implemented an accurate simulator with few sacrifices being made with respect to the model description. The simulator simultaneously solves the equations of the Bidomain Model and the forward problem. In this way iterating between the two solutions is avoided. Furthermore, special attention has be given to representing the ionic current accurately. To this end we have used the cell model of Luo–Rudy [20]. Efficient numerical techniques such as multigrid and adaptivity have been employed. The simulator is validated by simulations on simple and more anatomically correct geometries and the requirements on the discretization parameters are established.

2 The physiology of the problem

Blood enters the heart via the atria and are pumped back to the body by the contraction of the ventricles. The right ventricle supplies the blood to the lungs while the more powerful left

ventricle pumps blood into the rest of the body. The circuit is illustrated in Fig. 1.

The tissue of the ventricles and atria are composed of muscle fibers. These fibers are oblong like cylinders with a step-like surface that connects to neighboring fibers. Electrical current is lead from cell to cell through these connections and the direction of the current flow is therefore determined by the orientation of the fibers. This makes the myocardial tissue *anisotropic*, i.e. the electrical conductivity is not the same in all directions.

The individual muscle cells contract when they are stimulated electrically and they also pass the stimulus on to neighboring cells, thus stimulating the heart at one point creates a wave of depolarization throughout the heart. This wavefront is narrow typically thinner than one millimeter.

The propagation process is sped up by a special type of fibers which conducts the stimulus faster than normal muscle fibers, these are called Purkinje fibers. They originate from the atrioventricular(AV) node, which is located between the atria and the ventricles, and branch out to the ventricles. Electrical pulses travels along these fibers and at their endings the surrounding tissue is stimulated. As a result the depolarization is initiated simultaneously at multiple locations in the heart, resulting in a synchronized contraction of the muscle cells.
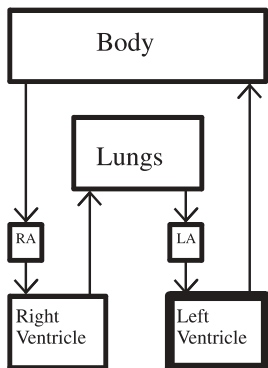
Fig. 1. The flow of blood through the body. The *thick line* around the left ventricle indicates the larger amount of muscle mass compared to the right ventricle. *RA* and *LA* represents the right and left atrium, respectively

2.1 Electrophysiology of the myocytes

The cell is delimited by the plasma membrane. The purpose of the membrane is to control the flow of substances into and out of the cell. The composition of the intra- and extracellular fluid differ, both chemically and electrically. In particular, the intracellular potassium concentration is much higher than the extracellular potassium concentration. This causes an outflow of potassium ions and consequently a difference in charge distribution. The charge gradient sets up a transmembrane potential.

Excitable cells like muscle cells and nerve cells differ from other cells in that they have the ability to change their transmembrane potential from the normal resting potential. Some of the ion channels in the membrane of excitable cells are controlled by gates which are sensitive to external stimulus. The permeability of the membrane is thus affected by changes in the external conditions. An increase of the transmembrane potential above the resting potential is called depolarization. This may occur for instance when sodium channels are opened and the positively charged sodium ions flow into the cell.

Up to a certain level the depolarization is graded, i.e. the greater the stimulus the greater the response. However, if the stimulus causes the cell to depolarize beyond the so-called threshold potential a different kind of reaction takes place, the action potential. The response is no longer graded but rather a cascade response. Voltage sensitive gates open up sodium channels, causing more ions to flow into the cell and making the transmembrane potential depolarize further. This causes the gates to become even more open and the influx increases further. This self-amplifying process continues past the point where the cell is completely depolarized and until a positive peak potential is reached. This is called the upstroke of the action potential and it lasts for only a few milliseconds. The aggregated effect of the upstrokes in all the ventricular myocytes is visible as the strongest signal in the ECG and it is termed the QRS-complex.

After the depolarization the cell has a large (intracellular) concentration of both sodium and potassium. The cell is repolarized when potassium gates open and potassium ions flow out of the cell. For the cardiac cells the action potential duration (APD) is about 200 ms. The repolarization is visible as the T-wave in the ECG. The Na-K pump contributes to the restoring of concentration gradients of both sodium and potassium. For myocardial cells the long APD is maintained by slow inward calcium currents. The cell membrane is also permeable to chloride ions, although their influence on the action potential is small under normal conditions.

3 The mathematical model

3.1 The Bidomain Model

In the Bidomain Model the cardiac tissue is divided into two spaces: the extracellular domain and the intracellular domain. Each domain is continuous and encompasses the whole myocardium, that is the domains have identical geometries and every point of the myocardium is found in both domains. The value of an entity defined in either space is interpreted as a volume averaged value.

Inside each domain the current flow is assumed to be purely resistive, this means that the current density J is proportional to the gradient of the potential u:

$$J = -M\nabla u .$$

Here M is the matrix representing the conductivities in the different directions. By conservation of current we have that the inflow in one domain must be the opposite of the outflow in the other domain, i.e.:

$$\nabla \cdot J_i = -\nabla \cdot J_e \tag{1}$$

where the subscripts i and e denotes the intra- and extracellular volume, respectively. The flow between the domains as expressed in (1) are referred to as the transmembrane current and denoted I_m. Per definition of I_m we have that

$$I_m = -\nabla \cdot J_i . \tag{2}$$

An alternative expression for I_m follows from the cable theory [14]. The membrane has the ability to both conduct and accumulate charge. This is modeled as an electrical circuit with a resistor and capacitor in parallel, see Fig. 2. The currents corresponding to each term are denoted the ionic current (I_{ion}) and the capacitive current (I_c). These currents are measured per unit area of surface membrane, while the transmembrane current is measured per unit volume. To convert between the two dimensions one must know the surface area-to-volume ratio, denoted χ. We then have:

$$I_m = \chi \left(I_{ion} + I_c \right) . \tag{3}$$

The capacitor is characterized by its capacitance C which is the ratio of the accumulated charge (q) to the potential difference over the capacitor (v), i.e

$$C = q/v . \tag{4}$$

In our setting v will be the difference between the intracellular and the extracellular potential, i.e.

$$v = u_i - u_e . \tag{5}$$

This difference is referred to as the transmembrane potential. An expression for the capacitive current is obtained by rearranging the terms in (4), divide by a time interval Δt and then go to the limit:

$$I_c \overset{\text{def}}{=} \lim_{\Delta t \to 0} \frac{\Delta q}{\Delta t} = C \lim_{\Delta t \to 0} \frac{\Delta v}{\Delta t} = C \frac{dv}{dt} \tag{6}$$
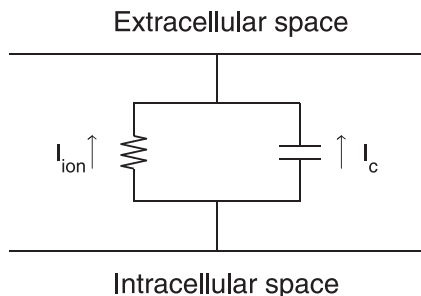
Unlike the current passing through an Ohmian resistor, the ionic current does not vary linearly with the transmembrane potential. This is due to the non-linear conductivity properties of the cell membrane described in Sect. 2.1. The ionic current is not only a function of the transmembrane potential but also of ionic concentration gradients and the state of the membrane. We put all these variables in one vector and denote it by s. We then have the relation

$$I_{ion} = I_{ion}(v, s) \tag{7}$$

where $I_{ion}(v, s)$ will be specified below.

Inserting (3) into (2) and eliminating u_i from (1) and (2) by using (5) we obtain the following coupled PDE system:

$$C\chi \frac{\partial v}{\partial t} + \chi I_{ion}(v, s) - \nabla \cdot (M_i \nabla v) = \nabla \cdot (M_i \nabla u_e)$$

$$\nabla \cdot ((M_i + M_e) \nabla u_e) = -\nabla \cdot (M_i \nabla v) \tag{8}$$

Extracellular space

Fig. 2. The membrane is modeled as a resistor and a capacitor coupled in parallel

The state vector s will vary throughout the myocardium just like v and u_e, i.e. it will be a function of position. Typically, s is governed by an ODE for each point in space so the system for $s(t, x)$ will be on the form

$$\frac{\partial s}{\partial t}(x) = F(t, s(t, x), v(t, x); x) \tag{9}$$

with an initial value

$$s(0, x) = s_0(x) .$$

Here F is the vector valued function defining the time derivatives of the state variables.

3.2 The ionic current

The appropriate expression for $I_{ion}(v, s)$ in (7) depends upon the type of species under study and also on the location within the myocardium. In our study we have chosen to use the model of Luo–Rudy [20] since it is well documented and very accurate. The additional variables of the model are

$$s = ([Na]_i, [K]_i, [Ca]_i, [Ca]_{JSR}, [Ca]_{NSR}, m, h, j, x, d, f) .$$

The terms in the square brackets represent ionic concentrations. Specifically, $[Na]_i$, $[K]_i$ and $[Ca]_i$ are the intracellular concentrations of sodium, potassium and calcium, respectively. The symbols $[Ca]_{JSR}$ and $[Ca]_{NSR}$ represents the concentration of calcium in two special compartments within the cell: The Junctional- and Network Sarcoplasmic Reticulum. The latter six variables are referred to as gating variables and they characterize the permeability of the cell membrane for different ions. They will be discussed below.

The time derivatives of the concentrations are proportional to the current flow of the specific current. For example the time rate of change for the sodium concentration is

$$\frac{d[Na]_i}{dt} = -c \cdot I_{Na,tot}$$

where c is a constant that depends upon the geometry of the cell and $I_{Na,tot}$ represents the net outward sodium current. This outflux is a sum of several currents, each corresponding to a specific type of channel in the membrane. The flux for the other ions are modeled in a similar way. The total ionic current is the sum of the three ionic currents crossing the membrane:

$$I_{ion} = I_{Na,tot} + I_{K,tot} + I_{Ca,tot}$$

See Sect. A.1 in the appendix for details.

The expressions for the currents through the different channels are derived by combining analytical consideration with measurements and the result can be quite esoteric. The following will give some of the background for the expressions.

One may divide the ionic channels into two different types, passive and active channels. The passive channels simply let ions pass according to the electro-chemical gradient of the ion. For these channels there exists an equilibrium potential where flux in one direction due to the concentration gradient is counterbalanced by a flux in the opposite direction

due to the electrical field generated by imbalance of charge. This potential is known as the Nernst equilibrium potential and is given by

$$v_X = \frac{RT}{zF} \ln \frac{[X]_o}{[X]_i}$$

where R is the gas constant, F is the Faraday constant, T is the absolute temperature and z is the valence of the generic ion X. $[X]_o$ and $[X]_i$ denote the extra- and intracellular concentrations, respectively. The passive channels thus have zero net flow when $v = v_X$. The current through a channel of this kind might look like

$$I = G(v - v_X)$$

where G is the conductance of the channel. However, the dependence on v need not be linear as long as the current is zero at the equilibrium. The correct form of the expression can only be determined through measurements.

The active channels move ions against their concentration gradient and are not restricted by the Nernst equilibrium. The energy may be taken from ATP (pumps) or the potential energy stored in form of concentration gradients of other ions (exchangers).

The conductance G might be a constant or depend upon ion concentration or the transmembrane potential. For some channels it has been shown that it also is time dependent. This dependency is modeled by the gating variables. They take on values in the interval [0, 1] and represent the openness of a channel. The actual conductance of a channel is calculated by multiplying the maximum conductance ($\overline{G}$) with the corresponding gating variable. The time rate of change for a generic gate g is given as

$$\frac{dg}{dt} = (g_\infty(v) - g) / g_\tau(v) . \tag{10}$$

The value of the gating variable approaches the steady state value g_∞ at a rate determined by g_τ. For numerical reasons it is favorable to express (10) as

$$\frac{dg}{dt} = \alpha_g(1 - g) - \beta_g g .$$

Here α_g represents the rate at which closed gates open and β_g represents the rate at which opened gates close.

The gating variables m, h and j are related to the fast inward sodium current i_{Na}, d and f are related to currents through a class of channels called L-type channels with the calcium current i_{Ca} being the most important. Finally, x is related to an outward potassium current, i_K. The definitions of α_g and β_g for $g = m, h, j, x, d, f$ are given in Sect. A.2.

3.3 Boundary conditions

The myocardial domain, denoted by H, is assumed to be embedded in a conductive medium which we will call the extracardiac domain and denote by D. The potential on D is denoted by u_D. This medium might be a torso or just a simple homogeneous and isotropic bath. Due to the cavities of the heart, the domain H will contain holes for physiological

correct geometries. Thus D can also represent one of these cavities depending on what part of the myocardial boundary we are considering. The computation of u_D is discussed below.

At the boundary between D and H the extracellular domain of the heart connects to the extracardiac tissue and thus u_e and u_D will refer to the same quantity so

$$u_e(x) = u_D(x), \quad x \in \partial H . \tag{11}$$

The most general assumption about the relationship between the current densities on the boundary is to allow for both extra and intra cellular current to pass out of the myocardial volume:

$$n \cdot J_D = n \cdot (J_e + J_i) . \tag{12}$$

Substituting for currents equation (12) can be rewritten as

$$n \cdot M_D \nabla u_D = n \cdot (M_i + M_e) \nabla u_e + n \cdot (M_i \nabla v) . \tag{13}$$

This assumption will have to be accompanied by a supplementary boundary condition in order for the equation system to be complete. There has been some debate regarding the appropriate condition [11]. Some argue that intracellular current does not leave the domain (e.g. $nM_i \cdot u_i = 0$) in that case equation (12) reduces to $n \cdot J_D = n \cdot J_e$. Another possibility is to invoke a condition on v directly. Colli Franzone et al. [5] suggest

$$n \cdot (M_i \nabla v) = 0 . \tag{14}$$

It can be argued for the physiological plausibility of this choice, in our setting however the main motivation is that of the two possibilities (14) leads to the most tractable form of the problem.

3.4 Anisotropy

Since the muscle fibers conduct current mainly along their lengths, the conductivity of the cardiac tissue is not isotropic. To simulate the propagation pattern of the wave front accurately, it is necessary to include the orientation of these fibers in the model. The introduction of fiber orientation leads to an anisotropic model. In the Bidomain Model this anisotropy is dealt with through the introduction of the conductivity tensors M_i and M_e. Following [4] we let

$$(a_1(x), a_2(x), a_3(x))$$

be a perpendicular set of vectors of unit length and with $a_1(x)$ lying along the fiber direction, see Fig. 3. Furthermore, let

$$M^* = \begin{bmatrix} \sigma_l & 0 & 0 \\ 0 & \sigma_t & 0 \\ 0 & 0 & \sigma_t \end{bmatrix} \tag{15}$$

be the local conductivity tensor, i.e. expressed with respect to the basis formed by (a_1, a_2, a_3). The conductivity along the fiber direction is σ_l (l for longitudinal) and the conductivity across the fiber direction is σ_t (t for transversal).
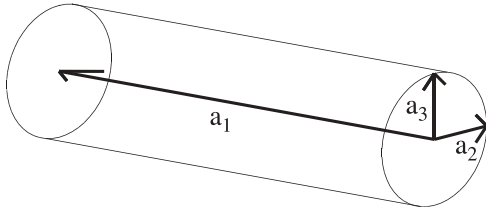
Fig. 3. The orientation of the local coordinate system of a single strand of fiber. The length of the arrows indicate the variation in conductivity in the different directions

For a potential gradient $p^* = (p_1, p_2, p_3)^T$ expressed in this local coordinate system the corresponding current vector will be

$$i^* = M^* p^* = (\sigma_l p_1, \sigma_t p_2, \sigma_t p_3)^T = (i_1, i_2, i_3)^T \ . \quad (16)$$

This vector is converted to global coordinates by

$$i = i_1 \boldsymbol{a}_1 + i_2 \boldsymbol{a}_2 + i_3 \boldsymbol{a}_3 = A i^* \quad (17)$$

where A is the matrix formed by taking the vectors $\boldsymbol{a}_1(x)$, $\boldsymbol{a}_2(x), \boldsymbol{a}_3(x)$ as columns. A potential gradient vector p expressed in global coordinates is mapped to local coordinates with the inverse mapping, that is $p^* = A^{-1} p$. Since A has perpendicular and normalized column vectors we have that $A^{-1} = A^T$ so the mapping is simply

$$p^* = A^T p \ . \quad (18)$$

Combining (16), (17) and (18) we get the relationship between a potential gradient and a current density vector, both expressed in global coordinates:

$$i = A M^* A^T p \quad (19)$$

and thus we define the global conductivity tensors by

$$M_i = A M_i^* A^T \quad \text{and} \quad M_e = A M_e^* A^T \quad (20)$$

where M_i^* and M_e^* is given as in (15) with (σ_l, σ_t) set equal to (σ_l^i, σ_t^i) and (σ_l^e, σ_t^e) respectively. The pair (σ_l^i, σ_t^i) refers to the conductivities in the intracellular domain and (σ_l^e, σ_t^e) refers to the conductivities in the extracellular domain.

The expression for the conductivity tensors in (20) can be simplified. A general element in M is

$$M_{ij} = \sigma_l a_1^i a_1^j + \sigma_t a_2^i a_2^j + \sigma_t a_3^i a_3^j$$
$$= (\sigma_l - \sigma_t) a_1^i a_1^j + \sigma_t \left(a_1^i a_1^j + a_2^i a_2^j + a_3^i a_3^j \right) \quad (21)$$

so

$$M = (\sigma_l - \sigma_t) \boldsymbol{a}_1 \boldsymbol{a}_1^T + \sigma_t A A^T$$
$$= (\sigma_l - \sigma_t) \boldsymbol{a}_l \boldsymbol{a}_l^T + \sigma_t I \quad (22)$$

where we have defined $\boldsymbol{a}_l = \boldsymbol{a}_1$.

3.5 Electrical potential outside the myocardium

The Bidomain Model only describes the electrical potentials in the myocardium. In order to simulate ECG measurements we also need to compute the potential distribution in the rest of the torso.

The properties of the tissue outside the heart are much simpler, and it is assumed to be neither excitable nor contain any current sources. It may therefore be modeled as a passive conductor. By the conservation of current we obtain the following model for the electrical potential in D:

$$\nabla \cdot (M_D \nabla u_D) = 0 \ , \quad x \in D \ . \quad (23)$$

The equation is valid for $D = L, R, T$ where L and R are the left and the right ventricle and T is the torso excluding the heart. The topology of a horizontal cross-section of the domains are shown in Fig. 4. The plane normal of the cross-section is in the head-to-toe direction and cuts the middle of the heart. Cross-sections taken at heights below or above the heart will contain a single domain. In between there will be two domains, the torso and the heart without the cavities. The matrix M_D is the conductivity tensor on the corresponding domain.
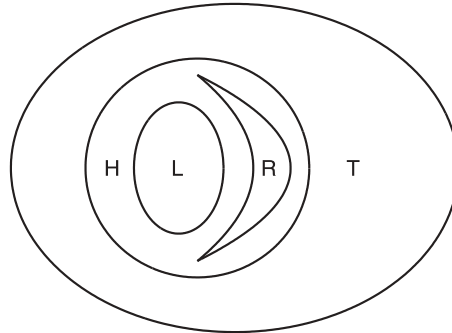
Fig. 4. A schematic horizontal cross section of the torso and the heart. H represents the myocardium, i.e. the heart muscle. L and R represent the left and right ventricles, respectively. T represents the torso. The four domains are disjoint and their union is denoted Ω

At the boundary of the torso a no-flow conditions is used:

$$n \cdot (M_T \nabla u_T) = 0 \ , \quad x \in \partial D \ . \quad (24)$$

The coupling to the heart is obtained through the boundary conditions on the myocardial surface as stated above in (11), (13), (14).

3.6 The parameters

The values of the parameters of the model are as follows:

$$\sigma_T = 2.39 \, \text{mS/cm}$$
$$\sigma_L = 6.0 \, \text{mS/cm}$$
$$\sigma_R = 6.0 \, \text{mS/cm}$$
$$\sigma_l^i = 3.0 \, \text{mS/cm}$$
$$\sigma_l^e = 2.0 \, \text{mS/cm}$$

$\sigma_t^i = 0.31525 \,\text{mS/cm}$

$\sigma_t^e = 1.3514 \,\text{mS/cm}$

$\chi = 2000 \,\text{cm}^{-1}$

$C = 1 \,\mu\text{F/cm}^2$ (25)

The conductivity parameters were found in Klepfer et al. [17], the surface area to volume ratio was found in Henriquez et al. [12] and the membrane capacitance was taken from Pollard et al. [22].

3.7 Summary of the model

The equations in L, R, T and the second equation in (8) for H all share the same structure, with the biggest difference being that the right hand side in (8) is non-zero. Due to the continuity conditions of the extracellular and extracardiac potential as stated in (11) and (13) it is possible to replace these four equations with a single equation, cf. [10] and [19] (page 37). This simplifies the implementation of the model considerably. We define Ω to be the union of all the domains, $\Omega = T \cup H \cup L \cup R$, and $u(x)$ to coincide with the different potentials on each subdomain:

$$
u(x) = \begin{cases} u_T(x), & \text{if } x \in T \\ u_e(x), & \text{if } x \in H \\ u_L(x), & \text{if } x \in L \\ u_R(x), & \text{if } x \in R \end{cases}
$$

The equation for u becomes

$$
\nabla \cdot (M\nabla u) = f, \quad x \in \Omega
$$
$$
n \cdot (M\nabla u) = 0, \quad x \in \partial\Omega (= \partial T)
$$

where

$$
f(x, v) = \begin{cases} -\nabla \cdot (M_i \nabla v) & \text{if } x \in H \\ 0 & \text{otherwise}, \end{cases} \quad\quad (26)
$$

and

$$
M(x) = \begin{cases} M_T(x), & \text{if } x \in T \\ M_i(x) + M_e(x), & \text{if } x \in H \\ M_L(x), & \text{if } x \in L \\ M_R(x), & \text{if } x \in R. \end{cases} \quad (27)
$$

With this simplification the system (8), (14), (23), (24) with (9) becomes

$$
H: \frac{\partial s}{\partial t} = F(t, s, v; x)
$$
$$
H: C\chi \frac{\partial v}{\partial t} + \chi I_{\text{ion}}(v, s) = \nabla \cdot (M_i \nabla (v + u))
$$
$$
\partial H: n \cdot (M_i \nabla v) = 0
$$
$$
\Omega: \nabla \cdot (M\nabla u) = f(x, v)
$$
$$
\partial\Omega: n \cdot (M\nabla u) = 0 \quad\quad (28)
$$

with f and M defined as in (26) and (27), respectively.

Above u is unique modulo a constant. To fix this constant we impose a Dirichlet condition in one of the computational nodes. We are only interested in gradients of u, hence the value of this constant is not significant.

4 A numerical method

4.1 Time discretization

In order to discretize (28) we introduce the timestep $t_n = n\Delta t = nT/N$ where N denotes the number of time steps and T is the duration of the simulation. At these time-levels we introduce the variables $u^n = u(t_n, x)$, $v^n = v(t_n, x)$ and $s^n = s(t_n, x)$.

The equations in (28) are a coupled system and should ideally be solved simultaneously. We have chosen to solve them sequentially thus applying a standard sequential operator splitting technique. The equations are solved in the following order:

1. Assume that u^n, v^n and s^n are known at time t_n
2. Compute s^{n+1} by solving

$$
\frac{\partial s}{\partial t} = F(t, s, v; x), \quad s(t_n, x) = s^n \quad \text{and} \quad v(t_n, x) = v^n
$$

for $t \in (t_n, t_{n+1}]$
3. Compute v^{n+1} in H by solving

$$
C\chi \frac{\partial v}{\partial t} + \chi I_{\text{ion}}(v^n, s^{n+1}) = \nabla \cdot (M_i \nabla v) + \nabla \cdot (M_i \nabla u^n).
$$

4. Compute u^{n+1} in Ω by solving

$$
\nabla \cdot (M\nabla u^{n+1}) = f^{n+1}
$$

where f^{n+1} is obtained by inserting v^{n+1} in (26).

In Step 2 the ODEs are integrated forward in time with internal time steps. There is an ODE problem for each node in space so in this spatial continuous description there is an infinite number of problems. When the space is discretized there will be one ODE problem for each node in the grid. If adaptivity is used in the time stepping, the work load of each problem will depend upon its location. In quiescent areas large time steps can be taken while small time steps are used in areas where the upstroke takes place.

In Step 3 we have evaluated the ionic term by using the previous update of the transmembrane potential. In this way the reaction-diffusion equation will become linear with respect to v and thus much easier to solve. The error committed by this approximation will depend upon the size of the time step taken. Solving with a fully implicit scheme may have permitted larger time steps to be taken but each step would be very costly. As described below we will use a semi-implicit technique and we have found that evaluating the ionic current with the previous update of the transmembrane potential has not led to any instability problems. In fact, the scheme seems to be unconditionally stable.

The time derivative in Step 3 is approximated by

$$
\frac{\partial v}{\partial t} \approx \frac{v^{n+1} - v^n}{\Delta t}
$$

which gives us the following time discrete equation:

$$
C\chi \frac{v^{n+1} - v^n}{\Delta t} + \chi I_{\text{ion}}(v^n, s^{n+1}) = \nabla \cdot (M_i \nabla v^{n+1})
$$
$$
+ \nabla \cdot (M_i \nabla u^n). \quad (29)
$$

The diffusive term $\nabla \cdot (M_i \nabla v)$ is evaluated at t_{n+1} yielding a semi-implicit equation. This scheme requires a linear system of equations to be solved at each time step. If $\nabla \cdot (M_i \nabla v)$ was evaluated at t_n instead the solution v^{n+1} could be calculated without solving a linear system, however smaller time steps would be needed to avoid a divergence of the solution algorithm. Collecting terms of v^{n+1} and v^n in (29) yields

$$v^{n+1} - \frac{\Delta t}{C\chi} \nabla \cdot \left(M_i \nabla v^{n+1}\right) = v^n + g^n \qquad (30)$$

where

$$g^n = \frac{\Delta t}{C\chi} \left(\nabla \cdot \left(M_i \nabla u^n\right) - \chi I_{\text{ion}} \left(v^n, s^{n+1}\right)\right) .$$

4.2 Spatial discretization

The PDE on each time steps is discretized using the finite element method with linear basis functions over the elements. The linear systems are solved using multigrid. The methods are described in [18].

4.3 The construction of the conductivity tensors

As shown in (22) the conductivity tensors are defined in terms of the direction of the muscle fibers of the heart. To define the tensor in a given point one must know the axis direction in that point. In practice the fiber direction are only known at some discrete locations. Denote the direction at n such locations by $a_1, a_2 \ldots a_n$. The direction at an arbitrary point x can be computed by a weighted average of these known directions

$$a^i(x) = \frac{\sum_{j=1}^n a_j^i e^{-\lambda d(x)_j^2}}{\sum_{j=1}^n e^{-\lambda d(x)_j^2}}$$

where the superscript i denotes the ith component of the vector. The function $d_j(x)$ is the distance from the given point x to location number j, and λ is a parameter controlling the relative weight of locations with different distances. The computed vector is normalized.

4.4 Adaptivity

In order to represent the narrow wave front of the depolarization accurately very small elements are required. The distribution of the transmembrane potential away from the wave front displays comparatively little variation and the requirements on the element size there are less strict. This fact can be exploited by using an adaptive grid.

The basic idea of any adaptive scheme is to increase the node density where it is most needed. In our context this is in the wave front. A possible strategy is to go through the elements of the coarsest grid and mark those elements which contains the wave front and then subsequently refine all marked elements. This will give rise to a new grid on which the process can be repeated. The scheme is illustrated in Fig. 5. Note that in the first grid none of the elements inside the square $[0, 2]^2$ are tagged since they do not contain the wave front,

however they are still refined. The refinement of these elements is necessary to obtain a legal grid, i.e. a grid where no node lies on an edge of another element. Similar effects are
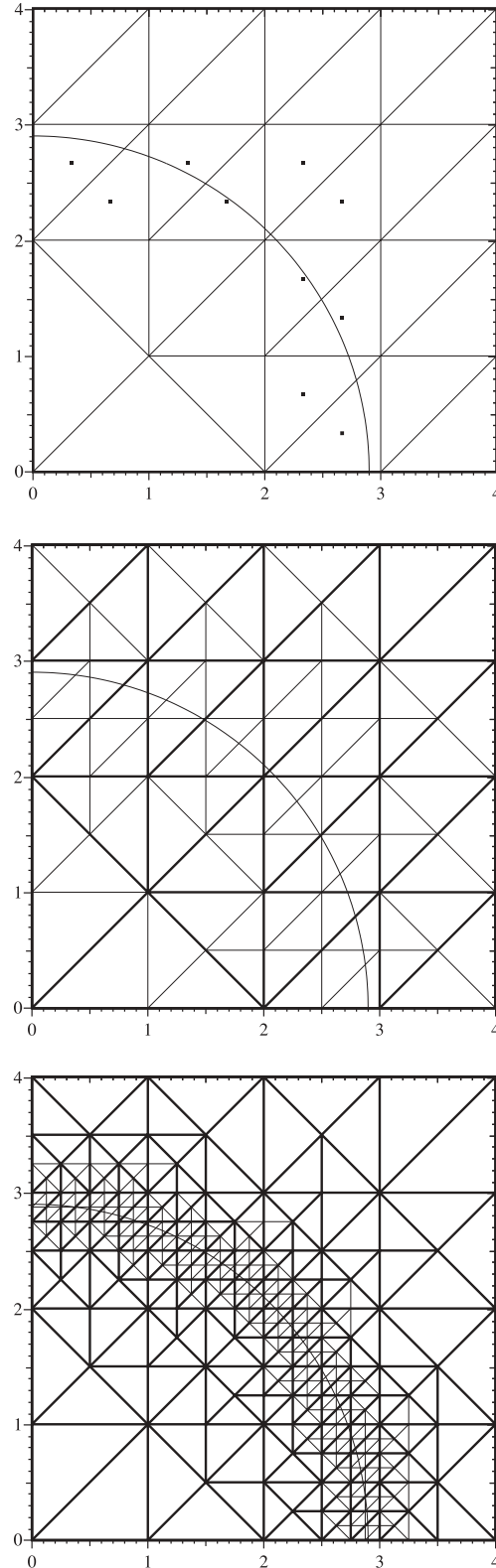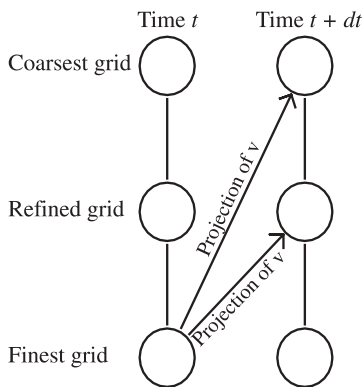

Fig. 5. *Top*: Coarse grid with elements containing the wave front (*curved line*) are marked with *dots*. *Middle*: The grid after refinement, original grid shown with *thick lines*. *Bottom*: The grid after two more refinements

also seen on the subsequent grids. On the finer grids the re-finements are located on a narrow strip around the wave front.
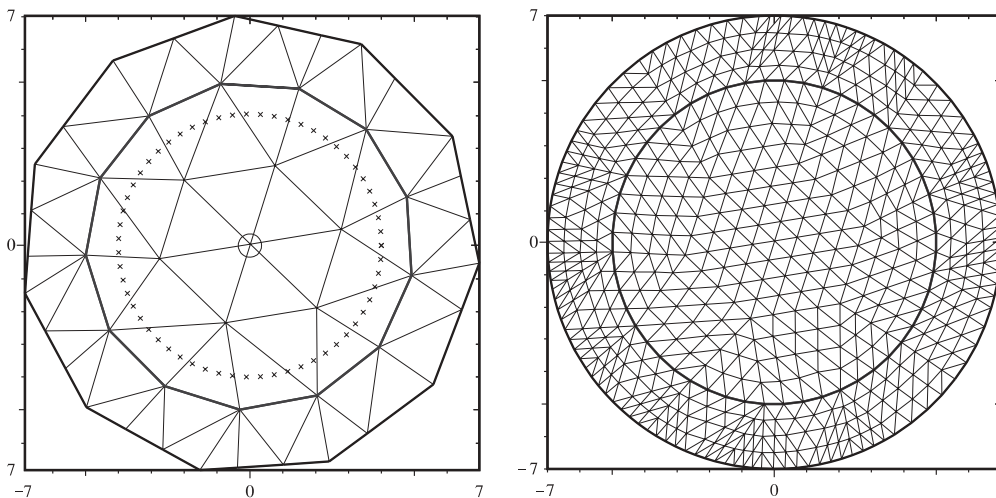
To determine if a given element contains the wave front it is sufficient to compute the differences in transmembrane potential v between all pairs of nodes in the element. If the wave front passes through an edge, the change over the pair of nodes defining that edge will be large. The element is marked if the change is above a given threshold. In our simulations we have chosen a small threshold (5 mV) to ensure that the wave front is maximally refined even on fine grids.

We use the solution from the previous time step, v^{n-1}, to compute the change in the solution over the elements in the coarser grids, as illustrated in Fig. 6. When the elements containing the wave front have been tagged a refined grid is computed. The solution v^{n-1} is then projected down to this re-fined grid and the process is repeated until the finest grid level has been reached.

The use of the previous solution to estimate the loca-tion of the wave front is justified by the small time step size compared to the movement of the wave front. With a typi-cal propagation speed of 1 mm/ms the wave front will move 0.125 mm during a time step of 0.125 ms. We will find in the next section that this is a sufficiently small time step and that the distance between the nodes of an element can be larger than 0.125 mm, thus the movement during a time step will

not be larger than a single element. Due to requirements for a legal grid, the high node density area will constitute a belt several elements thick around the wave front. The wave front of the solution computed on the new grid will therefore also lie inside this belt.

5 Simulations

5.1 Validation of the model on a simple 2D geometry

To validate the numerical results we would ideally like to compare the computed solution to an analytical solution and study the difference. Due to the complexity of the problem under study it is not feasible to compute an analytical solution and we have to use an indirect method to validate the model. We have chosen to formulate a problem to which the *shape* of the solution is known.

5.1.1 Geometry. A rotationally invariant problem has been formulated where the torso and the heart regions are con-centric disks with radius of 70 mm and 50 mm, respectively. Both regions are isotropic and homogeneous. The tissue is initially stimulated inside a disk at the center of the heart region. The applied current is sufficient to initiate the de-polarization process. The solution of this problem should be a wave front propagating in all directions with the same speed. The numerical solution of the problem should thus ap-proximate this behavior better and better as the grid becomes more refined.

The left panel in Fig. 7 shows the coarsest of this series of grids. The grid has been designed not to be rotationally in-variant as this would give a false impression of the accuracy of the method, since the reproduction of a rotationally invari-ant solution would be inherent due to the grid. As the grid is refined the nodes on the boundaries of the two domains are projected outwards to the circles they are approximating. In this way the discretization error of the representation of the circle tends towards zero as the grid is refined. The right panel in Fig. 7 shows the grid after two refinements.

In order to inspect the propagation speed in a quantita-tive way, the solution of the simulations has been recorded at 60 equally spaced sites 40 mm from the center as shown in

Fig. 6. The solution from the previous time step is projected onto the coars-est grid where the elements containing the wave front are refined, the process is repeated on the next grid etc.

Fig. 7. *Left*: The coarsest grid of the circle geometry. The bound-ary of Ω and H are drawn with *thick solid line*. The initial condi-tion is indicated by the *circle* in the center. Notice that the grid is not rotationally invariant. The *crosses* show the location of the tracking points. *Right*: The grid after two refinements, the boundary nodes are projected towards the circum-scribing circles

Fig. 7. Since the solution is radial, the solution at these locations should be identical.

5.1.2 Estimate of the required spatial resolution.
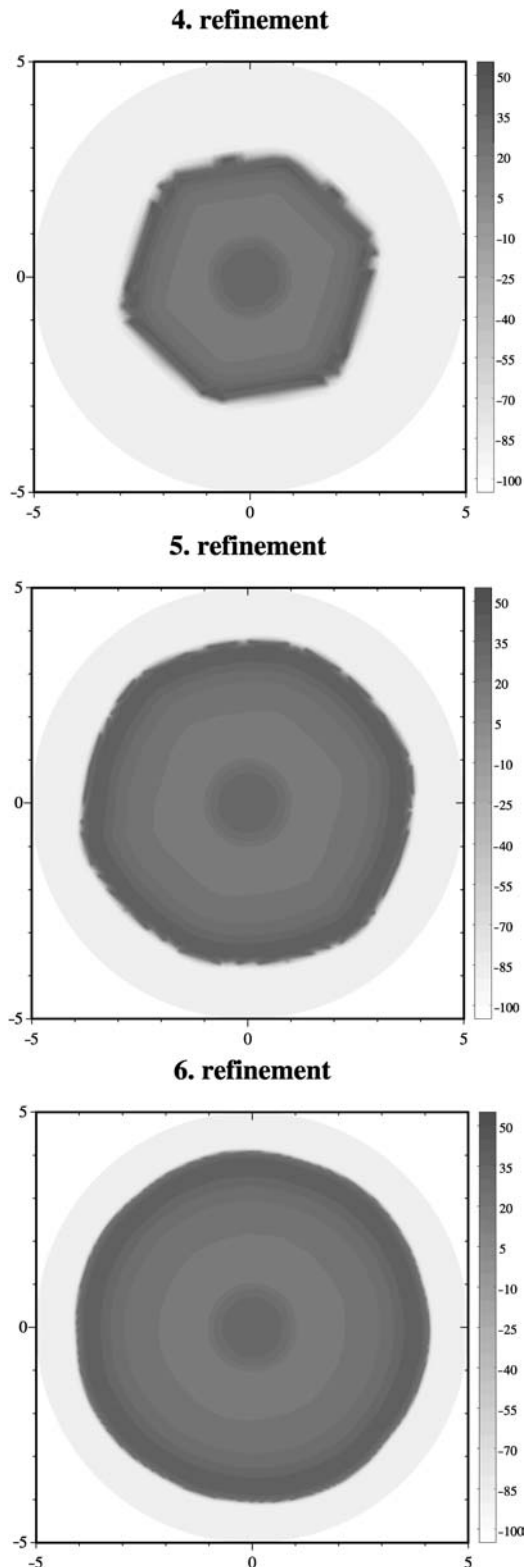Simulations of the depolarization phase have been performed with several

Fig. 8. The transmembrane potential after 30 s, plotted for simulations with three different levels of refinements

levels of refinement and for different sizes of the time step. Table 1 shows the number of nodes and elements for the different levels. To find the required node density the refinement level was varied as the time step was held constant. Preliminary experiments suggested that $\Delta t = 0.125$ ms was small enough to ensure reliable results. Figure 8 shows the transmembrane potential for three different levels of refinement at 30 ms after the initial stimulation. We see that the correct shape is not reproduced with relatively coarse grids but on finer grids the solution becomes more circular. The solution at refinement number 6 in Fig. 8 is hard to distinguish from a circle. By inspecting the solution at the tracking points it is easier to see the difference between the solution and a perfect circle. Note that for the exact solution, these curves coincide due to angular invariance. In the first row of Fig. 9 the transmembrane potential at the 60 tracking locations are shown for different levels of refinement. The figure clearly shows that the numerical solutions deviate from the correct rotationally invariant solution.

Table 2 contains some characteristic numbers of the activation times. From the table it is evident that the solution approaches a circular shape as the number of nodes increases. The standard deviation falls from 0.64 to 0.23 and then in the last refinement from 0.23 to 0.16. This last reduction indicates a somewhat slower convergence rate than what we could expect from a doubling of the node density. A halving of the error would be more in accordance with expectations. A possible reason for this behavior could be numerical diffusion, e.g. diffusion of the solution due to the numerical algorithm. Such unwanted diffusion will depend upon the element geometry and therefore break the symmetry in our simulations.

Table 1. The number of nodes in the two circular domains for different numbers of refinements. The number of elements increases by a factor of four with each refinement

| No of | Nodes | | Elements | |
refs	Heart	Torso	Heart	Torso
0	20	48	25	66
1	64	161	100	264
2	227	585	400	1056
3	853	2225	1600	4224
4	3305	8673	6400	16 896
5	13 009	34 241	25 600	67 584
6	51 617	136 065	102 400	270 336
7	205 633	542 465	409 600	1 081 344
8	820 865	2 166 273	1 638 400	4 325 376

Table 2. Some characteristics of the activation pattern shown in the first row of Fig. 9. The first column shows the number of refinements, the next shows the average time of activation, measured here as the moment where the potential becomes positive. The 'max($\Delta\tau$)' column is the difference between the activation times of the earliest and the latest tracking point, and finally the last column shows the standard deviation of the 60 activation times. All numbers are in milliseconds

Ref no	mean(τ)	max($\Delta\tau$)	sd(τ)
4	48.17	8.30	2.14
5	32.21	2.67	0.64
6	29.23	1.00	0.23
7	30.59	0.57	0.16
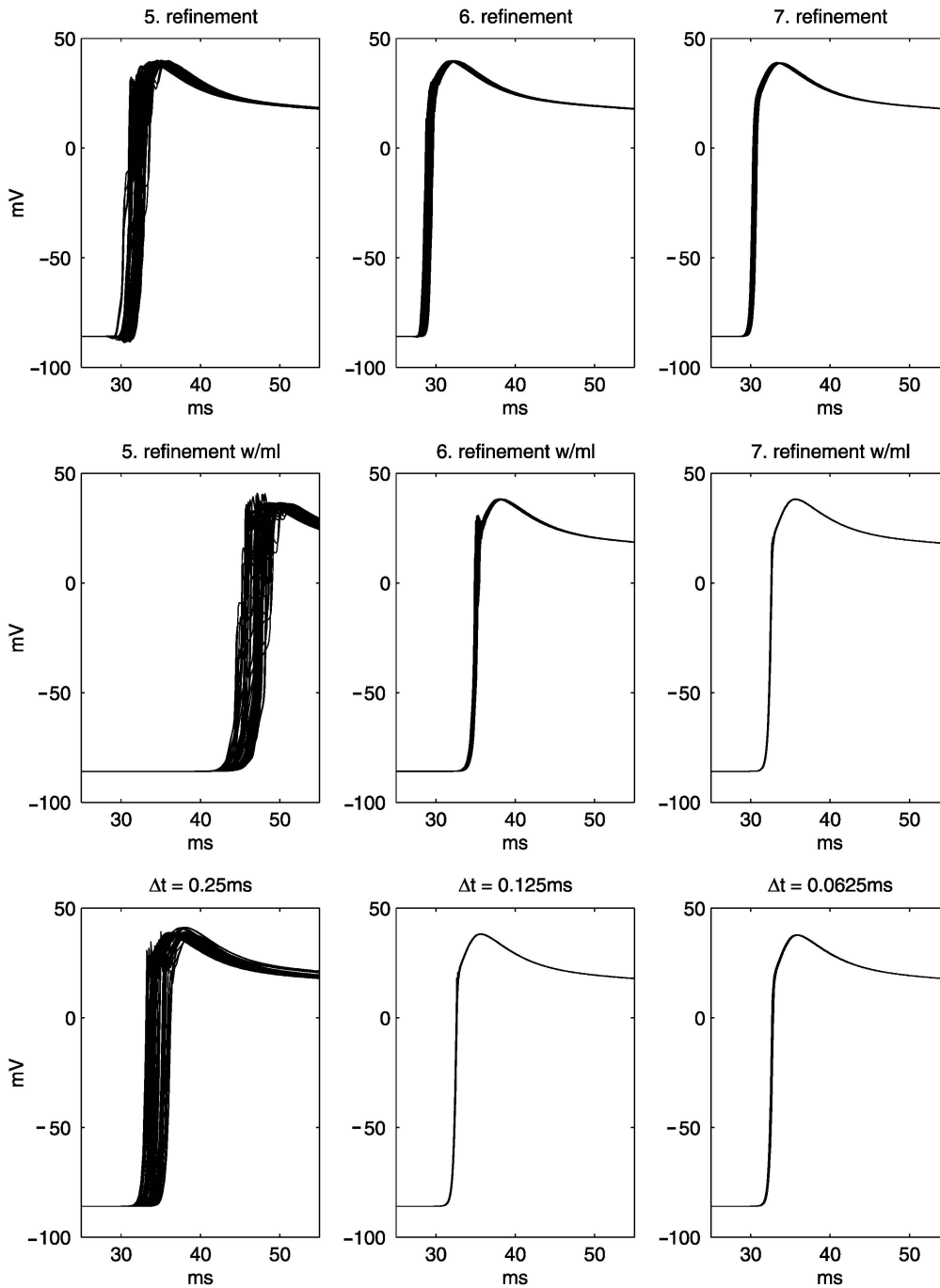
Fig. 9. The transmembrane potential at the tracking locations. The *first row* shows the action potential with the original computation, in the *second row* mass lumping and nodal evaluation has been used. The *last row* shows the effect of changing the time step

Mass lumping

Mass lumping is a technique to reduce the numerical diffusion described above. In short it is a manipulation of the stiffness matrix of the assembled linear system, where some off-diagonal components are moved onto the diagonal.

We have tried using this method in connection with a special choice of integration points (nodal as opposed to Gaussian) to further reduce the diffusion. The results can be seen in the the second row in Fig. 9 and also from Table 3. Due to reduced diffusion the node density required to sustain a traveling wave was higher with this technique. The coarsest simulation has therefore been left out of the table. In refine-

Table 3. The first four columns of the table are similar to Table 2, but the simulations are run with mass lumping and nodal evaluation in the numerical integration. Under the heading 'Spatial' the 'max($\Delta \hat{r}$)' column contains estimates of the maximal spatial deviation from a circular solution. The last column shows the resolution of the grid. The numbers of both columns are in millimeters. The corresponding activation patterns are shown in the second row of Fig. 9

Ref no	Temporal			Spatial	
	mean(τ)	max($\Delta \tau$)	sd(τ)	max($\Delta \hat{r}$)	Δx
5	46.99	3.86	0.98	2.46	0.78
6	35.15	0.66	0.14	0.56	0.39
7	32.61	0.12	0.033	0.11	0.20
8	32.05	0.07	0.016	0.066	0.098

ment number 6 and 7 the standard deviation goes from 0.98 to 0.14 and then down to 0.033, so the convergence towards the circular solution has been considerably improved by this technique. A further refinement (number 8) only halves the error. As argued for below, this indicates that the problem is sufficiently resolved already at refinement number 7.

Converting from the time domain to the spatial domain

The numbers in columns two to four in Table 3 are all in the time domain. In order to convert these figures into the spatial domain, we need an estimate for the propagation speed $\hat{v}$. If such an estimate is available then the maximal discrepancies in time of activation, $\Delta\tau$, can be translated into maximal variation in the radius of the depolarized tissue, $\Delta\hat{r}$, by

$$\Delta\hat{r} = \hat{v}\Delta\tau .$$

If constant propagation speed is assumed then

$$\hat{v} = r/\overline{\tau}$$

where r is the distance traveled by the front (30 mm). The fifth column of the table shows the estimated maximal spatial errors. The last column shows the resolution of the grid, it has been calculated in the following way:

$$\Delta x = \sqrt{\frac{\text{Area}}{\text{Number of nodes}}}$$

At the coarser grids the error in the solution is larger than the resolution of the grid, i.e. the solution is off by several elements. On refinement number 7 however the error drops below the grid resolution and the wavefront is located within the correct element. This means that the numerical solution is as circular as it can be on the given grid.

Conclusion

The experiments show that there is a gain in accuracy as the number of nodes is increased up to over 200 000 in the myocardial domain and that this density was required to achieve convergence to the proper solution. The corresponding resolution is 0.2 mm or 5 nodes/mm.

5.1.3 *Estimate of the required temporal resolution.* Above we concluded that reliable results were achieved at a spa-

tialresolution of $\Delta x = 0.2$ mm. We would now like to find the required temporal resolution Δt. Generally, Δt will depend upon the size of Δx. What we are interested in here is a reasonable value for Δt when we have $\Delta x = 0.2$ mm. To find this value we proceed in a similar way as above. The grid is kept fixed at refinement level 7 while the time step is varied.

The last row of Fig. 9 shows the tracking points for three choices of the time step, $\Delta t = \{0.25$ ms, 0.125 ms, 0.0625 ms$\}$. Clearly $\Delta t = 0.25$ ms is insufficient to obtain an accurate simulation. On the other hand, there is practically no difference between the solutions with $\Delta t = 0.125$ ms and $\Delta t = 0.0625$ ms, indicating that $\Delta t = 0.125$ ms is sufficient. The action potential uses about 0.5 ms to rise from the threshold potential to the peak potential. A time step of $\Delta t = 0.125$ ms ensures that the solution is updated several times during the upstroke.

### 5.2 A 2D simulation based on anatomical data

5.2.1 *Geometry.* In 2D we have also performed computations on a geometry based on anatomical data. The boundary of the heart was traced from an image of a human heart sliced in the horizontal plane [26]. The chosen slice is from the middle of the heart. The boundary of the torso was obtained from the Visible Human Man data [25]. This data set consists of a large number of high resolution photographs of cross sections of a male body.

The torso boundary was traced from the photograph corresponding to the same plane as the cardiac slice. The slice was then imposed upon the image and translated, scaled and rotated so that the traced slice matched the heart on the photograph. The reason why a different source was used for the heart data is that the contours of the chambers were not easily distinguishable in the Visible Human Man data. The traces of the boundaries are shown in the left panel of Fig. 10.

The fiber directions in the myocardium were not taken from measurements but set according to the known gross structure of this tissue. The fibers were set to run concentrically around the left ventricle. The fibers in the right ventricle runs in the same general direction as if it were cut out from the right hand side of the left ventricle. The three dimensional aspect of the fibers were not modeled. The right panel of Fig. 10 shows the basis directions as thick arrows and the interpolation throughout the domain. The interpolation was performed as described in Sect. 4.3
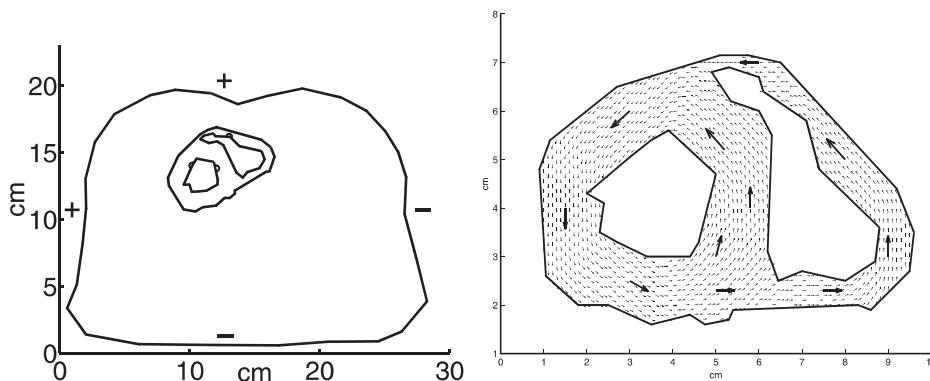
Fig. 10. *Left*: The boundary of the myocardium and the torso. The *dots* indicate the activation sites. The signs indicate the positions of ECG leads. *Right*: The fiber directions used in the model. The basis directions are shown with the *large arrows* while the interpolations used to compute the conductivity tensors are shown with *small arrows*
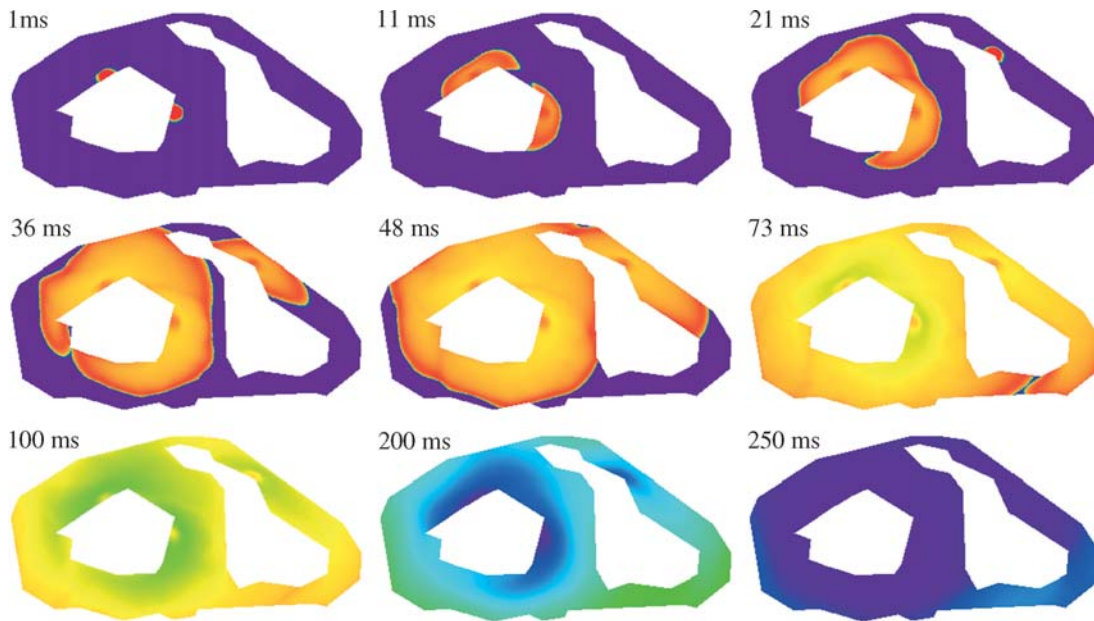
Fig. 11. Snapshots of the transmembrane potential, the time is indicated by the number on the left hand side of each plot. Animation at http://www.ifi.uio.no/~glennli/cvs/2D.mpeg

The activations sites were set according to Dürrer's activation map [6]. Myocardial activation was initiated at two locations in the left ventricle and 20 ms later at a site in the right ventricular wall as indicated in Fig. 10. There are more activation points in a real heart but since this is a 2D model only sites lying in the vicinity of the slice in question were included. Wave fronts originating from sites lying outside the slice could in principle depolarize tissue inside the slice before the fronts from the sites included. This possible effect is not included in the simulation.

The extracardiac potential has been tracked at two pairs of locations on the body surface, as shown in Fig. 10. The difference between the poles of each pair will then correspond to an ECG signal.

5.2.2 Results. The simulation includes both the depolarization and the repolarization phase, 300 ms in all. Figure 11 shows the transmembrane potential for some selected moments in time. The wave front radiates from the points of stimulation, first from the two sites in the left ventricle. This initiates a wave of depolarization that spreads concentrically around the left ventricle. The third activation site located in the right ventricle starts 20 ms later. After about 45 ms the wave fronts merge in the anterior part of the right ventricle. The depolarization is completed after 75 ms when the wave fronts merge in the posterior part of the right ventricle. The repolarization follows a similar but more protracted pattern. The myocardium is back to its resting potential 300 ms after the initial stimulation.

Figure 12 shows the evolution of the two ECG signals for two different levels of refinement, corresponding to refinement level 7 and 8 in Table 4 in Sect. 5.4.1. At refinement level 7 the node density is approximately 5 nodes per millimeter, which we in Sect. 5.1 concluded was sufficient. The signals in Fig. 12 are very similar which shows that there is a marginal difference between the two solutions. Both signals reproduce the QRS complex and the T-wave. There are

however some serious discrepancies between the simulated signals and the ones obtained from an actual measurement. First of all the amplitude of the signal is an order of magnitude larger than a typical measured signal. An explanation might be that we use a homogeneous torso which does not include the conductivity properties of the skin where the electrodes are placed.

Another striking feature of the signal is that it contains high frequency components not observed in ordinary surface ECGs. However, potentials recorded by placing electrodes in the myocardium display higher frequency components than the signal recorded at the body surface [15]. The difference in frequency content might be attributed to the fact that the signal recorded from surface electrodes are filtered due to the capacitor properties of the electrodes. Furthermore, the shape
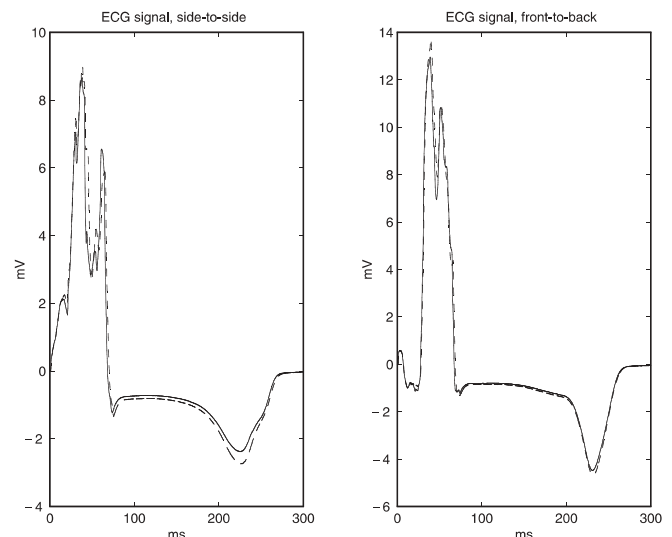
Fig. 12. ECG signals along the two axes. Results are shown for both a fine and a coarser simulation. Coarsest simulation shown with *dashed lines*

Table 4. Execution times for the simulations with the anatomical 2D geometry. N_P is the number of nodes in myocardium, N_E is the number of nodes in the entire torso (including the myocardium). 'ODE' is the time spent for solving the ODEs. Make-P: Assembly of the linear system of the parabolic equation. Solve-P: Solving the linear system arising from the parabolic equation. Make-E and Solve-E: Equivalent for the elliptic equation. All execution times are per time step and are reported in seconds. Simulation was performed in 300 ms in steps of 0.125 ms, giving a total of 2400 time steps

Ref. No	N_P	N_E	Total	ODE	Make-P	Solve-P	Make-E	Solve-E
5	4059	18 433	2.45	1.62	0.14	0.01	0.09	0.54
6	15 607	73 313	8.45	5.72	0.56	0.08	0.35	1.68
7	61 167	292 417	29.91	20.60	2.10	0.44	1.53	5.19
8	242 143	1 168 001	125.92	90.95	8.93	2.32	5.31	18.32

of the ECG signal depends upon the exact propagation of the wave fronts, one can therefore not hope to reproduce this signal accurately in a 2D simulation and with a simplified representation of the Purkinje network.

A third deviation from a normal ECG signal is the sign of the T-wave which is negative rather than positive. The reason for this is that in our simulations we have a fixed cell model throughout the myocardium while in reality the shape of the action potential varies. By not modeling this difference the repolarization will follow the same pattern as the depolarization, i.e. spreading from the inside to the outside of the heart, and with the potential gradients having opposite direction. If the APD is shorter near the outer surface, so that this part of the tissue will start to repolarize first, the wave front will follow the opposite pattern, thus inverting the sign of the T-wave.

5.3 A 3D simulation based on anatomical data

The geometry of the heart is taken from the data obtained by Nielsen et al. [21]. These data are unique in that, in addition to the description of the internal and external boundaries of the heart, it also contains the orientation of the muscle fibers throughout the myocardium.

The simulation has not taken advantage of all this data and it has been carried out on a much coarser grid than what we found is necessary from the numerical experiments of Sect. 5.1. The main point of including the simulation is to show that the simulator works fine also on irregular 3D geometries.

Figure 13 shows the propagation of the wave front. It is represented as an isopotential surface at 0 mV. The tissue is

stimulated initially in a single location located between the ventricles and the depolarization spreads out from there.

5.4 Time consumption

When solving the bidomain equations numerically three sub-problems are solved. These are the ODE equations to find the ionic current in each node, and the two PDEs of the bidomain system. Solving each PDE consists of two parts: assembling and solving the linear system of equations. Thus the whole problem can be divided into five separate tasks. In the following subsections we will study how the work load of the different parts vary with the problem size and with the spatial dimension. All execution times are obtained from simulations performed on a Linux PC with a 2 GHz Intel Xeon processor and with 2 Gb of memory.

5.4.1 The 2D case. Table 4 shows the time consumption of the 2D simulation presented in Sect. 5.2 with varying problem size. Below the workload of each subproblem has been ranked. The most CPU intensive task is listed first:

1. Solving the ODEs
2. Solving the linear system of the elliptic equation
3. Assembly of the parabolic equation
4. Assembly of the elliptic equation
5. Solving the linear system of the parabolic equation

The numbers in each row in the table are not entirely comparable since there are different number of nodes involved in the different subproblems. Specifically, the tasks under the headings "ODE", "Make-P" and "Solve-P" in Table 4 are
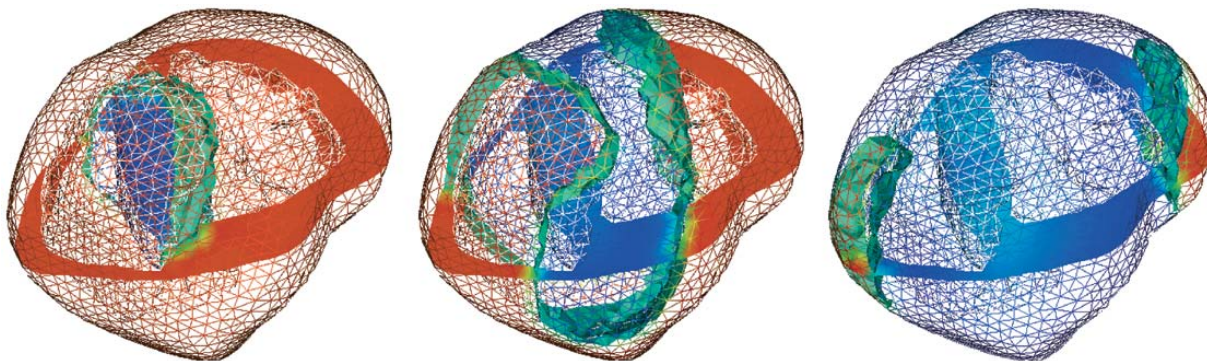
Fig. 13. The myocardium viewed from the front and above. The position of the wave front is represented as an isopotential surface at 0 mV, shown in *green*. An opaque transversal slice is also included. Polarized tissue is shown in *red* and depolarized tissue is shown in *blue*. Animation at http://www.ifi.uio.no/˜glennli/cvs/3D.mpeg

computed on the myocardial grid, while the last two are computed on the torso grid, which in this case is about four times as large.

The CPU-times shown in the table are averages over all time steps. The work load for some of the tasks however shows considerable variation. The ODE problem is harder to solve in the start and in the end of the cycle. This is when most of the heart has the resting potential. The work load is much smaller when the whole heart has been depolarized. For a single node most CPU time is consumed the moment when the wave front passes. The area of the wave front is so small however, that it does not contribute much to the total work. Thus the important aspect is not the area of the wave front (which also varies with time, unlike its thickness) but rather the amount of polarized tissue. The fact that the ODE system is stiffer in the polarized phase is not self evident. The reason is that the voltage dependent coefficient β_m of the m-gate of the fast inward current is very large during the resting potential, thus making this gating equation stiff and small time steps are therefore required. In the depolarized phase the m gate is still the stiffest equation but the coefficients are smaller so that the time steps can be larger.

The elliptic problem also varies in difficulty. The work load is highest during the time when the heart contains wave fronts. When there are no wave fronts present the changes from time step to time step will be less so that the initial guess, which is the previous solution, is good. Also, the coarse grid approximation of the solution will be better since the solution has only small high frequency components, yielding fewer multigrid iterations.

For the other three subproblems there is no systematic variation in time, except for the first time step where the time independent stiffness matrices are built.

5.4.2 The 3D case.
The CPU consumption for 3D simulations (not shown) is very similar to the 2D case. The only significant difference is that the workload per node for the Make routines are more costly in 3D. The reason is that there are more elements per node in 3D and that the workload per element is higher.

5.4.3 Growth in CPU time with problem size.
Table 5 shows the CPU-times from Table 4 divided by the number of nodes involved in the problem. In this way the numbers along each row becomes comparable and we can study the growth of work load as a function of the problem size. As expected the work needed to solve the ODEs in a single node is independent of the number of nodes in the problem. The same is true for the assembling of the linear systems for the two PDEs. The assembly routine consists of a single loop over all elements, and the work performed on a single element is independent of the problem size. Since the number of elements are almost proportional to the number of nodes the linear work growth is as expected.

The discretization of the PDEs yields linear equation systems with as many unknowns as the number of nodes in the grid. The linear systems are solved with the Multigrid Method [2, 9]. It has been proved [9] that the work load for elliptic equations is proportional to the number of unknowns. From the last row in Table 5 we see that the implemented solver performs in agreement with this result.

The only exception from the linear growth in work load is the solving of the parabolic equation. Although the rate of work increases faster for the parabolic case it is still an efficient solver. Furthermore, it constitutes the smallest part of the problem even on the finest grid. The linear speed up property is very desirable in our setting since the number of nodes required for a full scale 3D simulation will be extremely high. The work load for solving the parabolic equation may under these circumstances blow up and thus it might be necessary to find ways of solving the problem in linear time in order to avoid this.

5.5 Effect of adaptivity

The adaptive scheme suggested in Sect. 4.4 has been tested on the 2D problem with the geometry based on anatomical data.

5.5.1 The grid outside the myocardium.
The adaptive algorithm is based on the idea of refining the grid around the wave front of the transmembrane potential in the myocardium. Outside the myocardium the transmembrane potential is not modeled so the criterion can obviously not be used there. The extracardiac potential is governed by a different equation and the solution is qualitatively different. In particular the solution has no localized wave front. Furthermore, the solution depends upon the transmembrane potential in a global way, i.e. a movement of the wave front in the myocardium causes the extracardiac potential to change over the whole domain. Thus the solution varies substantially from time step to time step so the simple idea of the adaptive algorithm does not carry over to this part of the grid. Instead a fixed grid is used in the torso outside the myocardium.

The main point of the first simulation is to isolate the effect of adaptivity in the myocardium. Therefore the grid outside the myocardium is the same as the one used in the non-adaptive simulation we are comparing with, which corresponds to refinement number 7 in Table 4 and Table 5. Later in this section we will also try to simulate with a coarse grid in the torso.

5.5.2 CPU usage.
In row A and B of Table 6 we compare the time consumption with and without using adaptivity. The work spent on solving the ODEs is reduced, the same is

Table 5. Same as Table 4 but with execution times divided by the number of unknowns in addition to the number of time steps. All numbers are reported in microseconds

| Ref. No	N_P	N_E	ODE	Make-P	Solve-P	Make-E	Solve-E
5	4059	18 433	398.52	35.15	2.89	4.67	29.38
6	15 607	73 313	366.50	35.62	4.87	4.78	22.95
7	61 167	292 417	336.71	34.31	7.12	5.23	17.76
8	242 143	1 168 001	375.62	36.90	9.58	4.54	15.68

true for solving the parabolic system and the elliptic system. Since the number of unknowns is reduced, especially for the problems solved on the myocardial grid, this is as expected. For the assembling the situation is different. Since the stiffness matrix must be recomputed for each time step, the work load per node increases. For the parabolic equation this is more than counterbalanced by the reduction in the number of nodes. For the elliptic case the assembly process is more CPU intensive when using adaptivity. Again this is not surprising since the reduction of the number of nodes in the torso grid is marginal. However, under the 'Total' column in rows A and B we see that the increased cost of assembling does not outweigh the benefits of reducing the number of unknowns. It is not necessary to recompute all elementary stiffness matrices, but only those corresponding to new elements. By utilizing this fact it should be possible to construct assembling routines that handle the adaptivity efficiently. The workload connected to assembly could then be greatly reduced.

Table 6. Execution times for simulations on the accurate 2D geometry, with or without adaptivity. All numbers are per time step and measured in seconds. Simulation A is the second finest simulation from Table 4, simulation B is the same as A but with adaptivity on the myocardial grid, simulation C is the same as B but with a coarse grid outside the myocardium

Sim.	Total	ODE	Parabolic eq.		Elliptic eq.	
			Make	Solve	Make	Solve
A	29.91	20.60	2.10	0.44	1.53	5.19
B	13.60	4.70	0.54	0.10	4.02	4.26
C	2.08	1.11	0.18	0.02	0.20	0.57

5.5.3 Temporal variation in the number of nodes. The number of nodes in the myocardial grid is shown as a function of time in Fig. 14. In the initial steps the grid is forced to have a high resolution in order to represent the initial condition properly. Similarly, at $T = 20$ ms the adaptivity is turned off when the last activation site is started. The number of nodes falls sharply when the adaptivity is turned on. As the wave front spreads out the node density increases, because the area of the wave front increases. A peak is reached after
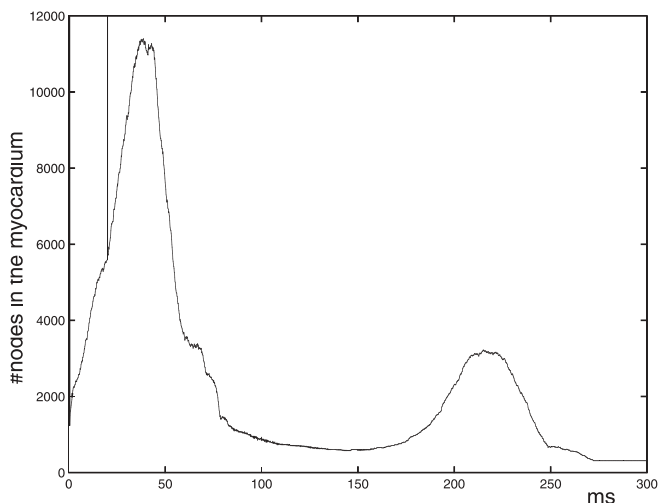
Fig. 14. The variation of the number of nodes throughout a simulation when using the adaptivity on the myocardial grid

40 ms. When the whole myocardium is depolarized the wave fronts disappear and the number of nodes falls quickly. The repolarization creates a wave front not unlike the depolarization, following the same pattern but being less steep. It is the propagation of this wave front that causes the last peak in the node density towards the end of the simulation. After this wave has passed through the domain the node density falls down to that of the coarsest grid in the multigrid hierarchy. Figure 15 shows the grid after 20 ms.
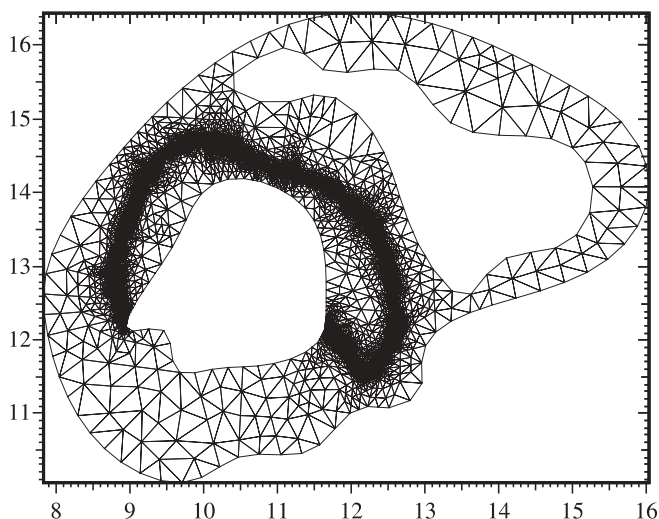
Fig. 15. The myocardial grid recorded 20 ms after initial stimulation. The node density is low on either side of the wave front. (Simulation number 2, coarse torso grid)

5.5.4 Simulation with a coarse torso grid. In the next simulation the elements outside the myocardium have not been refined, i.e. the coarsest grid is used. Row C of Table 6 shows the time consumption for this simulation. The tasks related to the elliptic problem (E-make and E-solve) are obviously solved much faster since the number of elements outside the myocardium is greatly reduced. For the tasks carried out exclusively on the myocardium there is also a substantial decrease in work load. In the first adaptive simulation the high density of nodes outside the myocardium also implied a high density of nodes on the myocardial side of the boundary. By having a coarse grid outside the myocardium the node density will initially be lower also in the myocardial grid. This explains the reduction in CPU time for solving the ODEs and the parabolic equation.

5.5.5 Quality of solutions. The reduced CPU times are of little use if the computed solutions are incorrect. The quality of the solutions can be evaluated by comparing the ECG signals. Figure 16 shows these signals for the three different simulations.

All simulations produce similar signals. The QRS complexes match up both with respect to amplitude and duration, although the signal of the last simulation cuts some of the steepest peaks. The T-wave sets in a bit earlier in the simulations using adaptivity. This means that the propagation speed is a bit faster on the adaptive grid during repolarization. In the transversal lead ECG there is a significant off-set in the ST-segment. This part of the signal is important when
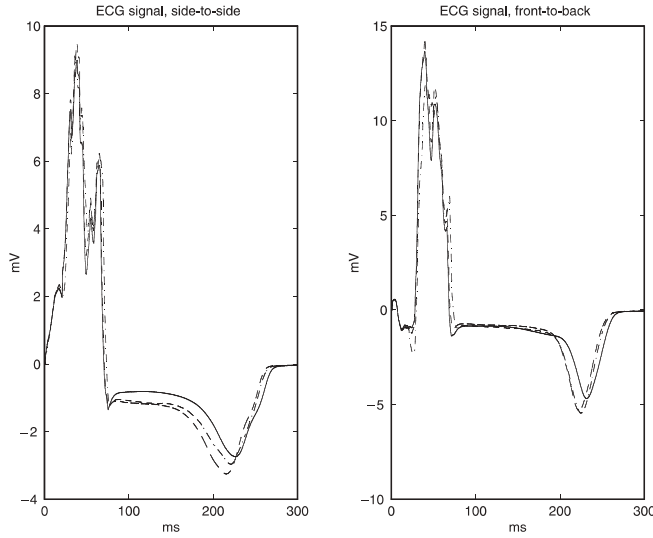
Fig. 16. The effect of using adaptivity, ECG signals for three simulation. Full grid both domains (*solid line*), adaptivity in myocardium and full grid outside (*dashed line*), adaptivity in myocardium and coarse grid outside (*dashed/dotted line*)

diagnosing ischemia and the inaccuracies introduced by adaptivity may be too large to make a quantitative study of these effects possible.

The ECG signal is a sensitive measure. Although there is some clear discrepancy in the signals, the solution obtained by using adaptivity might be sufficiently accurate in many circumstances. Certainly the activation sequence is well preserved.

The relatively little error committed when going from a fine to a coarse grid in the domain outside the myocardium shows that it is not necessary to have the same node density here as in the myocardium.

6 Discussion

The tests on the simple 2D geometry have shown that the simulator reproduces the basic features of the electrical properties of the myocardium. Current applied to an area with resting tissue caused depolarization. Subsequently, the depolarization spread out from this area and out to the rest of the myocardial tissue. From analytical considerations we knew that the solution of the these problems had to be rotationally invariant. This behavior was reproduced when the node density was about five nodes per millimeter and the time step no larger than an eighth of a millisecond.

On the geometries which were based on anatomical data the numerical solution could not be compared to features of an analytical solution since there were non available. On the other hand, the simulated situations were in these cases more comparable to what actually goes on in the heart so comparisons could be made directly to measurements. Only in 2D has it been possible to simulate with sufficient accuracy. In this case the propagation speed, the activation pattern and the duration of the depolarization process seemed plausible.

The repolarization phase has also been demonstrated. The inversion of the T-wave was attributed to the fact that identical models for the ionic current were used throughout the myocardium. If a more realistic distribution of APDs had been included the T-wave would show the normal behavior.

The growth in the CPU consumption was roughly linear with respect to the number of unknowns and the work load was less than one millisecond per unknown per time step. The only part of the problem that did not show the linear growth in the CPU consumption was the solving of the linear system of the parabolic equation. It constitutes of a small part of the problem even on the finest grids, but for fine 3D simulations this part of the problem may become significant. Solving the ODEs was the most CPU intensive part of the problem. The present implementation uses an explicit solver. In [24] implicit solvers are successfully applied to this problem.

The adaptive scheme yielded a significant reduced work load, but at the cost of a less accurate solution. An interesting result of the adaptivity simulations is that the grid outside the myocardium can have much larger elements than the ones in the myocardium. Even with many millimeters between the nodes, the generated ECG signals were very similar to the signals generated by using full resolution.

Appendix: The Luo–Rudy model

A.1 Ionic concentration change

The change in the ionic concentration is given by:

$$\frac{d[\text{Na}]_i}{dt} = -\frac{I_{\text{Na,tot}} \cdot A_{\text{Cap}}}{V_{\text{Myo}} \cdot F}$$

$$\frac{d[\text{K}]_i}{dt} = -\frac{I_{\text{K,tot}} \cdot A_{\text{Cap}}}{V_{\text{Myo}} \cdot F}$$

$$\frac{d[\text{Ca}]_i}{dt} = -\frac{I_{\text{Ca,tot}} \cdot A_{\text{Cap}}}{2 \cdot V_{\text{Myo}} \cdot F}$$

$$- (I_{\text{Up}} - I_{\text{Leak}}) \cdot \frac{V_{\text{NSR}}}{V_{\text{Myo}}} - I_{\text{Rel}} \cdot \frac{V_{\text{JSR}}}{V_{\text{Myo}}}$$

$$\frac{d[\text{Ca}]_{\text{JSR}}}{dt} = -I_{\text{Rel}} + I_{\text{Tr}}$$

$$\frac{d[\text{Ca}]_{\text{NSR}}}{dt} = I_{\text{Up}} - I_{\text{Leak}} + I_{\text{Tr}} \cdot \frac{V_{\text{JSR}}}{V_{\text{NSR}}}$$

where $A_{\text{Cap}} = 1.534 \times 10^{-4}$ is the capacitive membrane area, V_{Myo} is the volume of the myocardium, occupying 68% of the cell volume which is 38×10^{-6} μL. V_{NSR} and V_{JSR} occupy 92% and 8% of the SR respectively, and V_{SR} is 6% of the cell volume. $F = 96\,500$ is the Faraday constant. The currents related to SR are listed in Sect. A.4, the total transmembrane currents for each ions is as follows:

$$I_{\text{Na,tot}} = I_{\text{Na}} + 3I_{\text{NaCa}} + 3I_{\text{NaK}} + I_{\text{ns,Na}} + I_{\text{Nab}} + I_{\text{CaNa}}$$

$$I_{\text{K,tot}} = I_{\text{K}} + I_{\text{K1}} + I_{\text{Kp}} - 2I_{\text{NaK}} + I_{\text{ns,K}} + I_{\text{CaK}}$$

$$I_{\text{Ca,tot}} = I_{\text{Ca}} - 2I_{\text{NaCa}} + I_{\text{p(Ca)}} + I_{\text{Ca,b}}$$

The definition of the individual terms is listed in Sect. A.3

A.2 Gating variable coefficients

$$\alpha_m(v) = 0.32 \cdot (v+47.13) \big/ \left(1 - \mathrm{e}^{-0.1 \cdot (v+47.13)}\right)$$

$$\beta_m(v) = 0.08 \cdot \mathrm{e}^{-v/11}$$

$$\alpha_h(v) = \begin{cases} 0.135 \cdot \mathrm{e}^{(80+v)/(-6.8)} & \text{if } v < -40 \\ 0 & \text{otherwise} \end{cases}$$

$$\beta_h(v) = \begin{cases} 3.56 \cdot \mathrm{e}^{0.079 \cdot v} + 3.1 \times 10^5 \cdot \mathrm{e}^{0.35 \cdot v} & \text{if } v < -40 \\ 1 \big/ \left(0.13 \cdot \left(1 + \mathrm{e}^{(v+10.66)/(-11.1)}\right)\right) & \text{otherwise} \end{cases}$$

$$\alpha_j(v) = \begin{cases} \left(-1.2714 \times 10^5 \cdot \mathrm{e}^{0.2444 \cdot v} - 3.474 \times 10^{-5} \cdot \mathrm{e}^{-0.04391 \cdot v}\right) \\ \qquad \cdot \dfrac{v+37.78}{1+\mathrm{e}^{0.311 \cdot (v+79.23)}} & \text{if } v < -40 \\ \\ 0 & \text{otherwise} \end{cases}$$

$$\beta_j(v) = \begin{cases} 0.1212 \cdot \mathrm{e}^{-0.01052 \cdot v} \big/ \left(1 + \mathrm{e}^{-0.1378 \cdot (v+40.14)}\right) \\ \qquad \text{if } v < -40 \\ \\ 0.3 \cdot \mathrm{e}^{-2.535 \times 10^{-7} \cdot v} \big/ \left(1 + \mathrm{e}^{-0.1 \cdot (v+32)}\right) \\ \qquad \text{otherwise} \end{cases}$$

$$\alpha_x(v) = 7.19 \times 10^{-5} \cdot (v+30) \big/ \left(1 - \mathrm{e}^{-0.148 \cdot (v+30)}\right)$$

$$\beta_x(v) = 1.31 \times 10^{-4} \cdot (v+30) \big/ \left(-1 + \mathrm{e}^{0.0687 \cdot (v+30)}\right)$$

$$\alpha_d(v) = (0.035 \cdot (v+10)) \big/ \left(1 - \mathrm{e}^{-(v+10)/6.24}\right)$$

$$\beta_d(v) = \alpha_d \cdot \mathrm{e}^{-(v+10)/6.24}$$

$$\alpha_f(v) = f_\infty / f_\tau$$

$$\beta_f(v) = (1 - f_\infty) / f_\tau$$

$$f_\infty(v) = 1 \big/ \left(1 + \mathrm{e}^{((v+35.06)/8.6)}\right) + 0.6 \big/ \left(1 + \mathrm{e}^{(50-v)/20}\right)$$

$$f_\tau(v) = 1 \big/ \left(0.0197 \cdot \mathrm{e}^{-(0.0337 \cdot (v+10))^2} + 0.02\right)$$

A.3 Ionic currents

In this section [Ca] and $[\mathrm{Ca}]_{\mathrm{JSR}}$ refers to free concentration as opposed to total concentration elsewhere.

$$I_{\mathrm{Na}}(v, s) = \overline{G}_{\mathrm{Na}} \cdot m^3 \cdot h \cdot j \cdot (v - E_{\mathrm{Na}})$$

where $E_{\mathrm{Na}} = \dfrac{RT}{F} \cdot \log\left([\mathrm{Na}]_o / [\mathrm{Na}]_i\right)$

and $\overline{G}_{\mathrm{Na}} = 16$

$$I_{\mathrm{Ca}}(v, s) = d \cdot f \cdot f_{\mathrm{Ca}} \cdot \overline{I}_{\mathrm{Ca}}$$

where $f_{\mathrm{Ca}} = 1 \big/ \left(1 + \left([\mathrm{Ca}]_i / K_{m,\mathrm{Ca}}\right)^2\right)$,

$$K_{m,\mathrm{Ca}} = 0.6, \quad k = F \cdot \dfrac{vF}{RT}$$

and $\overline{I}_{\mathrm{Ca}} = 5.4 \times 10^{-4} \cdot 4 \cdot k$

$$\cdot \left(1 \cdot [\mathrm{Ca}]_i \cdot \mathrm{e}^{2 \cdot \frac{vF}{RT}} - 0.341 \cdot [\mathrm{Ca}]_o\right) \big/ \left(\mathrm{e}^{2 \cdot \frac{vF}{RT}} - 1\right)$$

$$I_{\mathrm{CaNa}}(v, s) = d \cdot f \cdot f_{\mathrm{Ca}} \cdot \overline{I}_{\mathrm{CaNa}}$$

where $\overline{I}_{\mathrm{CaNa}} = 6.75 \times 10^{-7} \cdot k$

$$\cdot \left(0.75 \cdot \left([\mathrm{Na}]_i \cdot \mathrm{e}^{\frac{vF}{RT}} - [\mathrm{Na}]_o\right)\right) \big/ \left(\mathrm{e}^{\frac{vF}{RT}} - 1\right)$$

$$I_{\mathrm{Ca,K}}(v, s) = d \cdot f \cdot f_{\mathrm{Ca}} \cdot \overline{I}_{\mathrm{CaK}}$$

where $\overline{I}_{\mathrm{CaK}} = 1.93 \times 10^{-7} \cdot k$

$$\cdot \left(0.75 \cdot \left([\mathrm{K}]_i \cdot \mathrm{e}^{\frac{vF}{RT}} - [\mathrm{K}]_o\right)\right) \big/ \left(\mathrm{e}^{\frac{vF}{RT}} - 1\right)$$

$$I_{\mathrm{K}}(v, s) = \overline{G}_{\mathrm{K}} \cdot X_i \cdot x^2 \cdot (v - E_{\mathrm{K}})$$

where $X_i = 1 \big/ \left(1 + \mathrm{e}^{(v-56.26)/32.1}\right)$

$$E_{\mathrm{K}} = \dfrac{RT}{F} \cdot \log\left(\left([\mathrm{K}]_o + P_{\mathrm{Na,K}} \cdot [\mathrm{Na}]_o\right) \big/ \right.$$
$$\left. \left([\mathrm{K}]_i + P_{\mathrm{Na,K}} \cdot [\mathrm{Na}]_i\right)\right)$$

and $P_{\mathrm{Na,K}} = 0.01833$, $\overline{G}_{\mathrm{K}} = 0.282 \cdot \sqrt{[\mathrm{K}]_o/5.4}$

$$I_{\mathrm{K1}}(v, s) = \overline{G}_{\mathrm{K1}} \cdot \mathrm{K1}_\infty \cdot (v - E_{\mathrm{K1}})$$

where $E_{\mathrm{K1}} = \dfrac{RT}{F} \cdot \log\left([\mathrm{K}]_o/[\mathrm{K}]_i\right)$,

$\overline{G}_{\mathrm{K1}} = 0.75 \cdot \sqrt{[\mathrm{K}]_o/5.4}$,

$\mathrm{K1}_\infty = \alpha_{\mathrm{K1}} / (\alpha_{\mathrm{K1}} + \beta_{\mathrm{K1}})$,

$\alpha_{\mathrm{K1}} = 1.02 \big/ \left(1 + \mathrm{e}^{0.2385 \cdot (v - E_{\mathrm{K1}} - 59.215)}\right)$,

and $\beta_{\mathrm{K1}} = \dfrac{0.49124 \cdot \mathrm{e}^{0.08032 \cdot (v - E_{\mathrm{K1}} + 5.476)} + \mathrm{e}^{0.06175 \cdot (v - E_{\mathrm{K1}} - 594.31)}}{1 + \mathrm{e}^{-0.5143 \cdot (v - E_{\mathrm{K1}} + 4.753)}}$

$$I_{\mathrm{Kp}}(v, s) = \overline{G}_{\mathrm{Kp}} \cdot \mathrm{Kp} \cdot (v - E_{\mathrm{K1}})$$

where $\mathrm{Kp} = 1 \big/ \left(1 + \mathrm{e}^{(7.488 - v)/5.98}\right)$

and $\overline{G}_{\mathrm{Kp}} = 0.0183$

$$I_{\mathrm{NaCa}}(v, s) = k_{\mathrm{NaCa}} \cdot \left(1 \big/ \left(K_{m,\mathrm{Na}}^3 + [\mathrm{Na}]_o^3\right)\right)$$
$$\cdot \left(1 \big/ \left(K_{m,\mathrm{Ca}} + [\mathrm{Ca}]_o\right)\right)$$
$$\cdot \left(1 \big/ \left(1 + k_{\mathrm{sat}} \cdot \mathrm{e}^{(\eta - 1) \cdot \frac{vF}{RT}}\right)\right)$$
$$\cdot \left(\mathrm{e}^{\eta \cdot \frac{vF}{RT}} \cdot [\mathrm{Na}]_i^3 \cdot [\mathrm{Ca}]_o - \mathrm{e}^{(\eta - 1) \cdot \frac{vF}{RT}} \cdot [\mathrm{Na}]_o^3 \cdot [\mathrm{Ca}]_i\right)$$

where $k_{\mathrm{NaCa}} = 2000$, $K_{m,\mathrm{Na}} = 87.5$, $K_{m,\mathrm{Ca}} = 1.38$,

$k_{\mathrm{sat}} = 0.1$, $\eta = 0.35$

$$I_{\mathrm{NaK}}(v, s) = \overline{I}_{\mathrm{NaK}} \cdot f_{\mathrm{NaK}} \cdot \left(1 \big/ \left(1 + \left(K_{m,\mathrm{Nai}}/[\mathrm{Na}]_i\right)^{1.5}\right)\right)$$
$$\cdot \left([\mathrm{K}]_o / ([\mathrm{K}]_o + K_{m,\mathrm{Ko}})\right)$$

where

$$f_{\mathrm{NaK}} = 1 \big/ \left(1 + 0.1245 \cdot \mathrm{e}^{-0.1 \cdot \frac{vF}{RT}} + 0.0365 \cdot \sigma \cdot \mathrm{e}^{-\frac{vF}{RT}}\right),$$

$$\sigma = (1/7) \cdot \left(\mathrm{e}^{[\mathrm{Na}]_o/67.3} - 1\right),$$

and $\overline{I}_{\mathrm{NaK}} = 1.5$, $K_{m,\mathrm{Nai}} = 10$, $K_{m,\mathrm{Ko}} = 1.5$

$$I_{\mathrm{ns,Na}}(v,s) = \overline{I}_{\mathrm{ns,Na}} \bigg/ \left[1 + \left(K_{m,\mathrm{ns(Ca)}}/[\mathrm{Ca}]_i\right)^3\right]$$

where $\overline{I}_{\mathrm{ns,Na}} = 1.75 \times 10^{-7}$

$$\cdot \frac{vF^2}{RT} \cdot \left(0.75 \cdot \left([\mathrm{Na}]_i \cdot e^{\frac{vF}{RT}} - [\mathrm{Na}]_o\right)\right) \bigg/ \left(e^{\frac{vF}{RT}} - 1\right),$$

and $K_{m,\mathrm{ns(Ca)}} = 1.2$

$$I_{\mathrm{ns,K}}(v,s) = \overline{I}_{\mathrm{ns,K}} \bigg/ \left[1 + \left(K_{m,\mathrm{ns(Ca)}}/[\mathrm{Ca}]_i\right)^3\right]$$

where $\overline{I}_{\mathrm{ns,K}} = 1.75 \times 10^{-7}$

$$\cdot \frac{vF^2}{RT} \cdot \left(0.75 \cdot \left([\mathrm{K}]_i \cdot e^{\frac{vF}{RT}} - [\mathrm{K}]_o\right)\right) \bigg/ \left(e^{\frac{vF}{RT}} - 1\right)$$

$$I_{\mathrm{p(Ca)}}(v,s) = \overline{I}_{\mathrm{p(Ca)}} \cdot \left([\mathrm{Ca}]_i \big/ \left(K_{m,\mathrm{p(Ca)}} + [\mathrm{Ca}]_i\right)\right),$$

$$\overline{I}_{\mathrm{p(Ca)}} = 1.15, \quad K_{m,\mathrm{p(Ca)}} = 0.5$$

$$I_{\mathrm{Ca,b}}(v,s) = \overline{G}_{\mathrm{Ca,b}} \cdot \left(v - E_{\mathrm{Ca,N}}\right)$$

where $E_{\mathrm{Ca,N}} = 0.5 \cdot \dfrac{RT}{F} \cdot \log\left([\mathrm{Ca}]_o/[\mathrm{Ca}]_i\right)$,

$$\overline{G}_{\mathrm{Ca,b}} = 0.003016$$

$$I_{\mathrm{Na,b}}(v,s) = \overline{G}_{\mathrm{Na,b}} \cdot (v - E_{\mathrm{Na}}), \quad \overline{G}_{\mathrm{Na,b}} = 0.00141$$

A.4 Calcium currents related to SR

$$I_{\mathrm{Up}} = \overline{I}_{\mathrm{Up}} \cdot \frac{[\mathrm{Ca}]}{[\mathrm{Ca}] + K_{m,\mathrm{Up}}}$$

where $K_{m,\mathrm{Up}} = 9.2 \times 10^{-4}$, $\overline{I}_{\mathrm{Up}} = 0.005$

$$I_{\mathrm{Leak}} = K_{\mathrm{Leak}} \cdot [\mathrm{Ca}]_{\mathrm{NSR}}$$

where $K_{\mathrm{Leak}} = \overline{I}_{\mathrm{Up}} \big/ \left[\overline{\mathrm{Ca}}\right]_{\mathrm{NSR}}$, $\left[\overline{\mathrm{Ca}}\right]_{\mathrm{NSR}} = 15$

$$I_{\mathrm{Tr}} = \left([\mathrm{Ca}]_{\mathrm{NSR}} - [\mathrm{Ca}]_{\mathrm{JSR}}\right) \big/ \tau_{\mathrm{Tr}}, \quad \tau_{\mathrm{Tr}} = 180$$

$$I_{\mathrm{Rel}} = G_{\mathrm{Rel}} \cdot ([\mathrm{Ca}]_{\mathrm{JSR}} - [\mathrm{Ca}])$$

I_{Rel} is only activated if the calcium concentration increase during the first 2 ms after the depolarization, denoted by $\Delta[\mathrm{Ca}]_2$, is larger than a given threshold $\Delta[\mathrm{Ca}]_{\mathrm{th}}$. The conductance G_{Rel} is therefore zero if $\Delta[\mathrm{Ca}]_2 < \Delta[\mathrm{Ca}]_{\mathrm{th}}$. It is given by:

$$G_{\mathrm{Rel}} = \begin{cases} \overline{G}_{\mathrm{Rel}} \cdot \dfrac{\Delta[\mathrm{Ca}]_2 - \Delta[\mathrm{Ca}]_{\mathrm{th}}}{K_{m,\mathrm{Rel}} + \Delta[\mathrm{Ca}]_2 - \Delta[\mathrm{Ca}]_{\mathrm{th}}} \left(1 - e^{-t/\tau_{\mathrm{on}}}\right) \\ \quad \cdot e^{-t/\tau_{\mathrm{off}}} \qquad \text{if } \Delta[\mathrm{Ca}]_2 > \Delta[\mathrm{Ca}]_{\mathrm{th}} \\ \\ 0 \qquad\qquad\qquad\quad \text{otherwise} \end{cases}$$

Here $t + 2$ ms is the time elapsed since the time derivative of the transmembrane potential reached its peak. The constants are $\overline{G} = 60$, $K_{m,\mathrm{Rel}} = 0.8$, $\tau_{\mathrm{on}} = \tau_{\mathrm{off}} = 2$ and $\Delta[\mathrm{Ca}]_{\mathrm{th}} = 0.18$.

A.5 Buffers

A buffer is a substance that can absorb a compound (in our case ions) when the concentration of that compound is high and which returns the compound to the solution if the concentration decreases. In this way the buffer prevents large concentration variation of that compound. The buffers included in the Luo–Rudy model are calmodulin and troponin in myoplasma and calsequestrin in JSR which all act as buffers for calcium.

The calcium concentration calculated by the model refers to the *total* amount of calcium both free and buffered, that is

$$[\mathrm{Ca}]_i = [\mathrm{Ca}]_{i,\mathrm{Tot}} = [\mathrm{Ca}]_{i,\mathrm{Free}} + [\mathrm{Ca}]_{i,\mathrm{Buffered}} \tag{A.1}$$

However, the $[\mathrm{Ca}]_i$ referred to in the current- and buffer-equations is the concentration of free calcium. The same subtle distinction also applies to $[\mathrm{Ca}]_{\mathrm{JSR}}$.

In JSR there is a single type of buffer, calsequestrin, and the amount of buffered calcium is given as a function of the amount of free calcium:

$$[\mathrm{Ca}]_{\mathrm{JSR,Buffered}} = [\mathrm{CSQN}] \frac{[\mathrm{Ca}]_{\mathrm{JSR,Free}}}{[\mathrm{Ca}]_{\mathrm{JSR,Free}} + K_{m,\mathrm{CSQN}}}$$

with $[\mathrm{CSQN}] = 10$ and $K_{m,\mathrm{CSQN}} = 0.8$.

The amount of buffered calcium in the myoplasma is given by:

$$[\mathrm{Ca}]_{i,\mathrm{Buffered}} = \mathrm{Ca}_{\mathrm{TRPN}} + \mathrm{Ca}_{\mathrm{CMDN}}$$

$$= [\mathrm{TRPN}] \frac{\mathrm{Ca}_{i,\mathrm{Free}}}{\mathrm{Ca}_{i,\mathrm{Free}} + K_{m,\mathrm{TRPN}}}$$

$$+ [\mathrm{CMDN}] \frac{\mathrm{Ca}_{i,\mathrm{Free}}}{\mathrm{Ca}_{i,\mathrm{Free}} + K_{m,\mathrm{CMDN}}}$$

The constants are $[\mathrm{TRPN}] = 70$, $K_{m,\mathrm{T}} = 0.5$, $[\mathrm{CMDN}] = 50$ and $K_{m,\mathrm{C}} = 2.38$.

References

1. Beeler, G.W., Reuter, H.: Reconstruction of the action potential of ventricular myocardial fibres. J. Physiol. 268, 177–210 (1977)
2. Bramble, J.H.: Multigrid methods. England: Longman Scientific & Technical 1993
3. Colli Franzone, P., Guerri, L.: Spreading of exitation in 3D models of the anisotropic cardiac tissue: 1. Validation of the Eikonal model. Math. Biosci. 113, 145–209 (1993)
4. Colli Franzone, P., Guerri, L., Tentoni, S.: Mathematical Modeling of the Excitation Process in Myocardial Tissue: Influence of Fiber Rotations on Wavefront Propagation and Potential Field. Math. Biosci. 101, 155–235 (1990)
5. Colli Franzone, P., Guerri, L., Rovida, S.: Wavefront propagation in an activation model of the anisotropic cardiac tissue: asymptotic analysis and numerical simulations. J. Math. Biol. 28, 121–176 (1990)
6. Dürrer, D., van Dam, R.T., Freud, G.E., Janse, M.J., Meijler, F.L., Arzbaecher, R.C.: Total excitation of the isolated human heart. Circulation 41, 899–912 (1970)
7. FitzHugh, R.A.: Impulses and physiological states in theoretical models of nerve membrane. Biophys. J. 1, 445 (1961)
8. Geselowitz, D.B., Miller, W.T.: A bidomain model for anisotropic cardiac muscle. Ann. Biomed. Eng. 11, 191–206 (1983)
9. Hackbusch, W.: Multi-Grid Methods and Applications. Berlin, Heidelberg, New York: Springer 1995
10. Hackbusch, W.: Elliptic Differential Equations. Berlin, Heidelberg, New York: Springer 1992

11. Henriquez, C.S.: Simulating the Electrical Behavior of Cardiac Tissue Using the Bidomain Model. Crit. Rev. Biomed. Eng. 21, 1–77 (1993)

12. Henriquez, C.S., Muzikant, A.L., Smoak, K.: Anisotropi, fibre curvature and bath loading effects on activation in thin and thick cardiac tissue preparations. J. Cardiovascular Electrophysiology 7, 424–444 (1996)

13. Huiskamp, G.: Simulation of Depolarization in a Membrane-Equation-Based Model of the Anisotropic Ventricle. Trans. Biomed. Eng. 45, 847–855 (1998)

14. Jack, J.J., Nodel, D., Tsien, R.W.: Electric current flow in excitable cells. Oxford: Clarendon Press 1983

15. Josephson, M.E.: Clinical Cardiac Electrophysiology. 2nd edn. Philadelphia/London: Lea & Febiger 1993

16. Keener, J.P.: A eikonal equation for action potential propagation in myocardium. J. Math. Biol. 29, 629–651 (1991)

17. Klepfer, R.N., Johnson, C.R., Macleod, R.S.: The Effects on Inhomogeneities and Anisotropics on Electrocardiographic Fields: A 3D FE Study. IEEE Trans. Biomed. Eng. 44, 706–719 (1997)

18. Langtangen, H.P.: Computational Partial Differential Equations Numerical Methods and Diffpack Programming. Berlin, Heidelberg, New York: Springer 1999

19. Lines, G.T.: Modeling the electrical activity of the heart – A bidomain model of the ventricles embedded in a torso. Dr. thesis no 13. Department of Informatics, University of Oslo, 1999. URL: http://www.ifi.uio.no/~glennli/thesis.pdf

20. Luo, C.H., Rudy, Y.: A dynamic model of the cardiac ventricular action potenial. Circ. Res. 74, 1071–1096 (1994)

21. Nielsen, P.M.F., Le Grice, I.J., Smaill, B.H., Hunter, P.J.: Mathematical model of geometry and fibrous structure of the heart. Am. J. Physiol. 260, 1365–1378 (1991)

22. Pollard, A.E., Hooke, N., Henriquez, C.S.: Cardiac Propagation Simulation. Crit. Rev. Biomed. Eng. 20, 171–210 (1992)

23. Rogers, J.M., McCulloch, A.D.: A Collocation-Galerkin FEM of Cardiac Action Potential Propagation. IEEE Trans. Biomed. Eng. 41, 743–757 (1994)

24. Sundnes, J., Lines, G.T., Tveito, A.: Efficient solution of ordinary differential equations modeling electrial activity in cardiac cells. Math. Biosci. 172, 55–72 (2001)

25. The Visible Human Project. URL: http://www.nlm.nih.gov/research/visible/visible_human.html

26. Zych, D.K.: Hjertets elektriske aktivitet modelert ved hjelp av elementmetoden. Master thesis in Norwegian. Department of informatics. University of Oslo, 1994